Effects of nuclear surface polarization on exotic cluster radioactivity in trans-lead nuclei

Zhen Wang [1,*] and Zhongzhou Ren[1,2,†]

[1]*School of Physics Science and Engineering, Tongji University, Shanghai 200092, China*
[2]*Key Laboratory of Advanced Micro-Structure Materials, Ministry of Education, Shanghai 200092, China*

Radioactive dynamics of unstable nuclei are subject to nuclear deformation. The experimentally identified cluster radioactivities in the trans-lead region are reexamined using an improved density-dependent cluster model in this work, where the role of deformation is fully taken into account. Especially, the effects of nuclear diffuseness polarization [Phys. Rev. C **88**, 064327 (2013)], a nontrivial distortion of the nuclear surface due to deformation, are further investigated in the calculations of cluster radioactivity as well. In the present work, we generalize a new unified form of deformation-dependent diffuseness in the nuclear density distribution by introducing an adjustable parameter, whose sign determines the specific surface polarization mode, while its amplitude together with the deformation parameters handle the surface polarization degree of a deformed nucleus. Within this diffuseness correction, we first examine the improved model's capability of investigating the properties of cluster radioactivity. The experimental half-lives are found to be well reproduced with a factor of ≈ 3. Sequentially we consider three different surface polarization modes for the emitted cluster in the calculations and compare their impacts on the properties of cluster radioactivity. Distinct features and effects of these three surface polarization modes are presented in detail. As a result, it is found that the three different surface polarization modes may alter the geometry of daughter-cluster interactions, leading to a fluctuation of the cluster radioactivity half-lives. It is expected this work can serve as a helpful reference for both the experimental and theoretical studies of nuclear structures in the future.

I. INTRODUCTION

The instability of nuclei leads to radioactivity. Since the first discovery of radioactivity by Becquerel in 1896, various radioactivities have been observed experimentally, among which α decay and spontaneous fission are the two main disintegration processes in heavy and superheavy unstable nuclei [1]. Between these two above-mentioned decay modes, there is also a special case named cluster radioactivity, in which an unstable heavy or superheavy nucleus would spontaneously emit a charged particle heavier than α particle (^{4}He nucleus) while lighter than the fragment in spontaneous fission. Pioneering work was done by Săndulescu, Poenaru, and Greiner in 1980, who first theoretically predicted the cluster radioactivity of heavy nuclei based on the superasymmetric fission model (SAFM) [2]. Subsequently, the cluster radioactivity was experimentally confirmed by Rose and Jones in 1984, via the observation of ^{14}C emission from ^{223}Ra [3]. Since then, emissions of various clusters (e.g., ^{14}C, ^{20}O, $^{22,24-26}$Ne, ^{28,30}Mg, ^{32,34}Si, etc.) from heavy or superheavy nuclei, decaying to daughters around the doubly magic nucleus, have been detected and confirmed experimentally [4–6]. As compared with α decay, the branching ratios of these cluster radioactivities are extremely small, thereby making very long

half-lives. It is therefore critical to have a trustworthy method to estimate the cluster decay rates accurately.

A full microscopic quantum-mechanical treatment of cluster radioactivity is extremely difficult due to the complications of quantum many-body problems. In general, cluster radioactivity is phenomenologically studied in theory from two perspectives, namely, the "α-decay like" theory [7–15] and the "fission like" theory [2,16–19], as an intermediate case between α decay and spontaneous fission. The former treats the cluster radioactivity as a quantum tunneling process of a preformed heavy cluster, whereas the latter considers it to be a consecutive evolution of geometrical shapes that reaches the scission configuration after passing over the Coulomb barrier. Additionally, many semi-empirical formulas have also been developed to study cluster radioactivity [8,20–23]. Experimental half-lives are found to be approximately reproduced in a satisfactory manner by all these models or formulas. Among the above-mentioned models, the density-dependent cluster model (DDCM), which takes the nuclear density distributions and the effective nucleon-nucleon interactions into account, has been proven to be successful in explaining the properties of α decay [24–30], proton emission [31], two-proton radioactivity [32,33], and cluster radioactivity [7,9]. Recently, we enhanced the DDCM by incorporating the anisotropic nuclear surface diffuseness of deformed daughter nucleus [34–36] into α-decay calculations, as well as explored the effects of nuclear diffuseness anisotropy and polarization on favored α decay [28,29]. It was shown that the diffuseness

*wang_zhen@tongji.edu.cn
†zren@tongji.edu.cn

polarization would change the shape of nucleon density profile and effective α-core interactions and could even lead to an increase of about 20% in the α-decay half-life of a nucleus with large deformation. The improved model known as DDCM+ significantly improved the accuracy over DDCM. Inspired by our previous works [28,29], we make a further extension of DDCM+ to investigate the properties of cluster radioactivity in this work.

Differing from the α particle, which is a doubly magic nucleus, deformation of the cluster emitted from heavy or superheavy nuclei is usually not negligible and should be considered in calculations. Nontrivial distortion of the nuclear surface thus occurs due to the deformation. In our previous works on α decay [28,29], the surface polarization in the deformed heavy system, i.e., the diffuseness reduces along the elongated axis while increasing along the compressed axis, is addressed in DDCM+ by using a deformation-dependent diffuseness correction. The situation for the emitted cluster which is a light system, however, becomes more complicated than that in a heavy nucleus. As demonstrated in Ref. [35], the systematic tendency of surface polarization in the deformed heavy system can hardly be discovered in the light systems through the SkM* and Sly4 energy density functional calculations. Instead, various surface polarization modes emerge in the light systems. Therefore, motivated by Refs. [34,35] and our previous work [28,29], we attempt to explore the effects of nuclear surface anisotropy and polarization on the properties of cluster radioactivity in this work. Especially, the various impacts resulting from the different surface polarization modes will be discussed in detail.

The remaining parts of this paper are organized as follows: Relevant details of the theoretical framework are presented and discussed in Sec. II. A series of calculated results including a detailed comparison of different polarization modes are presented in Sec. III. In addition, the effects of nuclear surface polarization on cluster radioactivity are somewhat discussed as well. A summary and sequential conclusions are given in Sec. IV.

II. THEORETICAL FRAMEWORK

A. The improved density-dependent cluster model (DDCM+)

The cluster emitter is treated in DDCM+ as a binary spherical-deformed system of the cluster (heavier than ^{4}He) interacting with the daughter nucleus after the cluster is assumed to be preformed at the surface of parent nucleus. In previous works of α decay, the α cluster is considered to be spherical, while the daughter nucleus is usually assumed to be deformed [25,28,29]. However, the situation of cluster radioactivity differs slightly from that of α decay. For the exotic cluster radioactivity, the daughter nucleus is often the doubly magic nucleus (i.e., ^{208}Pb) or a nucleus in its neighborhood, which is spherical or weakly deformed, while the deformation of the emitted cluster cannot be negligible [9,11,13]. Thus, in the present work, the axially symmetric deformation of the emitted cluster is taken into account, as well as the daughter nucleus is assumed to be spherical for simplification. The daughter-cluster system is shown in Fig. 1.
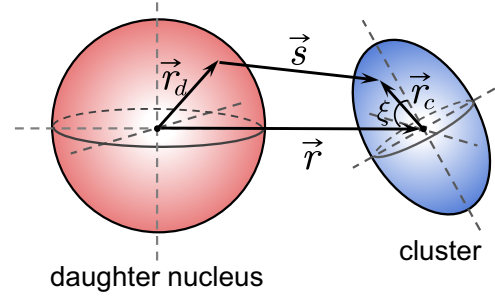

FIG. 1. Schematic illustration of coordinate systems used in the double-folding form interactions between the spherical daughter nucleus and deformed cluster. ξ is the orientation angle of the symmetry axis of the deformed cluster with respect to the vector connecting the center of masses of the two interacting nuclei.

The total interaction between the emitted cluster and the residual daughter nucleus consisting of nuclear potential $\mathcal{V}_N(r, \xi)$, Coulomb potential $\mathcal{V}_C(r, \xi)$ and centrifugal potential is given by

$$\mathcal{V}(r, \xi) = \mathcal{V}_N(r, \xi) + \mathcal{V}_C(r, \xi) + \frac{\hbar^2}{2\mu r^2} l(l+1), \quad (1)$$

where ξ is the orientation angle of the symmetry axis of the deformed cluster, $\mu = m_c m_d / (m_c + m_d)$ is the reduced mass of daughter-cluster system, l is the angular momentum carried by the emitted cluster. As the spin-parity of the ground state for the even-even cluster is 0^+, the conservation laws of angular momentum and parity yield [37]

$$|I_i - I_f| \leqslant l \leqslant I_i + I_f, \quad \pi_i = (-1)^l \pi_f, \quad (2)$$

where $I_{i,f}$ and $\pi_{i,f}$ are the spins and parities of the initial (denoted by i) and final (denoted by f) states, respectively. Then we adopt the minimum one among all possible l values verifying Eq. (2) in our calculations. The nuclear and Coulomb potential are performed through the double-folding procedure [38], which are

$$\mathcal{V}_N(r, \xi) = \lambda(\xi) \int d\vec{r}_c \int d\vec{r}_d \rho_c(\vec{r}_c) v(|\vec{r}_c + \vec{r} - \vec{r}_d|) \rho_d(\vec{r}_d),$$

$$\rho_c(\vec{r}_c) = \rho_c^p(\vec{r}_c) + \rho_c^n(\vec{r}_c), \quad \rho_d(\vec{r}_d) = \rho_d^p(\vec{r}_d) + \rho_d^n(\vec{r}_d),$$
$$(3)$$

and

$$\mathcal{V}_C(r, \xi) = \frac{e^2}{4\pi\varepsilon_0} \int d\vec{r}_c \int d\vec{r}_d \frac{\rho_c^p(\vec{r}_c) \rho_d^p(\vec{r}_d)}{|\vec{r}_c + \vec{r} - \vec{r}_d|}. \quad (4)$$

In Eqs. (3) and (4), $\lambda(\xi)$ is the strength factor of the nuclear potential depth at each orientation angle ξ, which is determined by reproducing the decay energy for the quasibound state in subsequent calculations. $\rho_c^{p,n}(\vec{r}_c)$ and $\rho_d^{p,n}(\vec{r}_d)$ denote the proton (denoted by p) and neutron (denoted by n) density distribution for the cluster and daughter nucleus, respectively. $s = |\vec{r}_c + \vec{r} - \vec{r}_d|$ is the relative separation between the two interacting nucleons in the daughter-cluster system, while the strength of M3Y-Reid nucleon-nucleon interaction $v(s)$ is

given as [39]

$$
\nu(s) = 7999.00 \frac{\exp(-4.0s)}{4.0s} - 2134.25 \frac{\exp(-2.5s)}{2.5s}
$$
$$
- 276[1 - 0.005(E_c/A_c)]\delta(\vec{s}), \tag{5}
$$

where E_c/A_c represents the kinetic energy per nucleon of the emitted cluster.

The density distribution of the protons and neutrons for daughter nucleus and the cluster are described by the two-parameter Fermi (2pF) form

$$
\rho_{c,d}^{\tau}(\vec{r}_{c,d}) = \frac{\rho_{c,d}^{\tau_0}}{1 + \exp\left[\dfrac{|\vec{r}_{c,d}| - \mathcal{R}^{\tau}(\theta)}{a^{\tau}(\theta)}\right]}, \tag{6}
$$

with $\tau_{(0)} = p_{(0)}$ or $n_{(0)}$. The half-radius parameter is given by

$$
\mathcal{R}^{\tau}(\theta) = \mathcal{R}_0^{\tau}\left[1 + \sum_{i=2,4,6} \beta_i Y_{i,0}(\theta)\right]. \tag{7}
$$

β_i ($i = 2, 4, 6$) in Eq. (7) represent the multipole deformation parameters, whose values for the emitted cluster are mainly taken from FRDM2012 [40] or Ref. [41], whereas they are assumed to be zero for the daughter nucleus in present work. $Y_{l,m}(\theta, \phi)$ is the spherical harmonics, the azimuth angle ϕ is implied in Eq. (7) and hereafter due to the axial symmetry of the nucleus. In DDCM+, we take the surface anisotropy and polarization effect into account by replacing the isotropic diffuseness parameter with the anisotropic one as [28,29]

$$
a^{\tau}(k', \theta) = a'(k', \theta)\sqrt{1 + \left[\frac{1}{\mathcal{R}^{\tau}(\theta)}\frac{d\mathcal{R}^{\tau}(\theta)}{d\theta}\right]^2}, \tag{8}
$$

in which the factor $a'(k', \theta)$ is given by

$$
a'(k', \theta) = a_0^{\tau}[1 + k'\beta_2 Y_{2,0}(\theta)]. \tag{9}
$$

Here, k' is an adjustable parameter handling the specific mode and degree of the nuclear surface polarization, and we will explicitly discuss it in Sec. III B. The similar expressions to Eq. (9) have also been proposed in Refs. [11,35,36,42].

The values of $\mathcal{R}_0^{\tau}$ and a_0^{τ} entering Eqs. (7) and (9) are estimated by the São Paulo parametrization with [43]

$$
\mathcal{R}_0^p = 1.81Z^{\frac{1}{3}} - 1.12 \text{ fm}, \; a_0^p = 0.47 - 0.000\,83Z \text{ fm},
$$
$$
\mathcal{R}_0^n = 1.49N^{\frac{1}{3}} - 0.79 \text{ fm}, \; a_0^n = 0.47 - 0.000\,46N \text{ fm},
$$
$$
\tag{10}
$$

respectively, which consider the differences between proton and neutron density distribution.

Once the nuclear and Coulomb potentials are constructed via the above procedure, the partial decay width of cluster radioactivity can be determined by numerically solving the quasibound Schrödinger equation, which is given by [9,14,44]

$$
\Gamma(\xi) = \frac{\hbar^2 k}{\mu} \frac{|\Psi_l(R, \xi)|^2}{G_l(\eta, kR)^2 + F_l(\eta, kR)^2} \approx \frac{\hbar^2 k}{\mu} \frac{|\Psi_l(R, \xi)|^2}{G_l(\eta, kR)^2}. \tag{11}
$$

In Eq. (11), $G_l(\eta, kr)$ and $F_l(\eta, kr)$ are the irregular and regular Coulomb wave function with the wave number being $k = \sqrt{2\mu Q_c}/\hbar$, η is the Sommerfeld parameter, and $\Psi_l(r, \xi)$ is the radial wave function at each certain orientation angle, respectively. The distance R should be chosen beyond the range of nuclear potential, and the final result is not sensitive to the choice of R. The approximation made in the last term of Eq. (11) is based on the fact that the half-lives of cluster radioactivity hereto observed are usually longer than 10^{10} s, indicating the imaginary part of the resonance energy (i.e., decay width) is extremely small, thus one could use energies and wave functions that are real instead without significant loss of accuracy [14,44].

The internal nodes in the radial wave function are determined by the well-known Wildermuth-Tang condition [45]

$$
\mathcal{G} = 2n + l = \sum_{i=1}^{A_c}\left(g_i^{A_c + A_d} - g_i^{A_c}\right), \tag{12}
$$

which approximately accounts for the Pauli-blocking effect, ensuring the nucleons in the emitted cluster occupy the physically allowed orbits. In Eq. (12), A_c (A_d) is the mass number of the emitted cluster (daughter nucleus), $g_i^{A_c + A_d}$ are the oscillator quantum numbers of the nucleons forming the cluster required to ensure that the cluster is completely outside the shell occupied by the daughter nucleus, and $g_i^{A_c}$ are the internal quantum numbers of the nucleons in the emitted cluster [46]. In the present work, the values of g_i are taken as $g_i = 4$ for nucleons with $50 \leqslant Z, N < 82$, $g_i = 5$ for nucleons with $82 \leqslant Z, N < 126$, and $g_i = 6$ for nucleons with $N \geqslant 126$. These values correspond to the $4\hbar\omega$, $5\hbar\omega$, and $6\hbar\omega$ harmonic-oscillator shells, respectively. Given the values of $\mathcal{G}$ and l, the number of nodes n in the radial wave function $\Psi_l(r, \xi)$ can then be determined.

Subsequently, the total decay width of cluster radioactivity thus can be obtained by averaging the partial decay width over the different orientations as

$$
\Gamma = \frac{\int_0^\pi \Gamma(\xi)\sin\xi \, d\xi}{\int_0^\pi \sin\xi \, d\xi} = \frac{1}{2}\int_0^\pi \Gamma(\xi)\sin\xi \, d\xi. \tag{13}
$$

Finally, the half-life of cluster radioactivity T_c reads

$$
T_c = \hbar \ln 2/(P_c \Gamma), \tag{14}
$$

where P_c denotes the preformation probability of the heavy-cluster in the parent nucleus. Similar to the case of α decay, microscopical calculation on the cluster preformation probability is still a pending problem as well, thus phenomenological estimates on P_c are often used in various cluster radioactivity calculations [7]. Based on the available experimental data, the preformation probability P_c is found to be related to the size of the cluster and the daughter nucleus. With these factors in mind, we choose an empirical formula to estimate P_c as [14]

$$
\log_{10} P_c = a\sqrt{\tilde{\mu} Z_c Z_d} + b, \tag{15}
$$

where $\tilde{\mu} = A_c A_d/(A_c + A_d)$, Z_c and Z_d are the proton numbers of the emitted cluster and daughter nucleus, respectively. The parameters a and b can be determined by fitting the extracted P_c values from the experimental data.

B. Unified decay formula for cluster radioactivity

The expression of the unified decay formula (UDF) for cluster radioactivity proposed by Ni *et al.* [8] is given as

$$\log_{10} T_{1/2} = c Z_c Z_d \sqrt{\frac{\tilde{\mu}}{Q_c}} + d \sqrt{\tilde{\mu} Z_c Z_d} + h. \qquad (16)$$

In Eq. (16), $\tilde{\mu}$, Z_c, and Z_d denote the same quantities in Eq. (15), and Q_c is the decay energy.

The values of c, d, and h are taken from Ref. [8] as follows:

$$c = 0.38617,$$
$$d = -1.08676,$$
$$h_{e-e} = -21.37195,$$
$$h_{o-A} = -20.11223. \qquad (17)$$

Here, different values of parameter h are adopted for even-even and odd-A nuclei, respectively, to reflect the hindrance in different kinds of nuclei, i.e., the hindrance of centrifugal barrier and so on. In some empirical formulas on α decay [47,48], the terms related to angular momentum l are often included explicitly to account for the hindrance of the centrifugal barrier, which could significantly improve the accuracy in calculating α-decay half-lives. Unlike the case of α decay, however, the emitted cluster in cluster radioactivity has relatively larger mass compared with an α particle. Moreover, the Coulomb barrier also becomes much higher than that in α decay. As a result, the centrifugal barrier plays a minor role in cluster radioactivity [14]. With this in mind, the hindrance of centrifugal barrier can be approximately involved in the parameter h by taking different values for each kind of nuclei, which could simplify the form of the UDF without any significant loss of accuracy in calculating half-lives of cluster radioactivity.

III. NUMERICAL RESULTS AND DISCUSSIONS

A. Half-lives of the exotic cluster radioactivity in trans-lead nuclei

Before analyzing the impacts of nuclear surface polarization, we first look at DDCM+'s capability of investigating the exotic cluster radioactivity in this section. In the present work, a total of 22 heavy-cluster emissions with certain half-lives and branching ratios are selected, and only those ground-state-to-ground-state transitions are considered in our calculations. We temporarily set the value of k' in Eq. (9) as $k' = 0$ in this section, corresponding to the case proposed by Bohr and Mottelson [34], to calculate the half-lives of cluster radioactivity ranging from ^{14}C up to ^{34}Si. As known, one of the most important inputs in DDCM+ is decay energy. Here, the decay energy Q_c is extracted from Ref. [50] by taking the relation

$$Q_c = \Delta M(Z, A) - \Delta M(Z_d, A_d) - \Delta M(Z_c, A_c), \qquad (18)$$

with $\Delta M(Z, A)$, $\Delta M(Z_d, A_d)$, and $\Delta M(Z_c, A_c)$ being the mass excesses of parent nucleus, daughter nucleus, and emitted cluster, respectively. The experimental uncertainty of decay energy σ_{Q_c} is given by

$$\sigma_{Q_c}^2 = \sigma_{\Delta M}^2(Z, A) + \sigma_{\Delta M}^2(Z_d, A_d) + \sigma_{\Delta M}^2(Z_c, A_c), \qquad (19)$$

with $\sigma_{\Delta M}(Z, A)$, $\sigma_{\Delta M}(Z_d, A_d)$, and $\sigma_{\Delta M}(Z_c, A_c)$ being the corresponding experimental uncertainty of $\Delta M(Z, A)$, $\Delta M(Z_d, A_d)$, and $\Delta M(Z_c, A_c)$, respectively [50]. Then there are only the cluster preformation factors P_c to be determined. We extracted the values of P_c via the ratio between the experimental and calculated decay widths:

$$P_c^{\text{extr}} = \Gamma_{\text{expt}}/\Gamma_{\text{theo}}, \qquad (20)$$

where the experimental decay width Γ_{expt} is related to the experimental half-life T_c^{expt} by the well-known relationship $\Gamma_{\text{expt}} = \hbar \ln 2/T_c^{\text{expt}}$, while the calculated decay width Γ_{theo} is obtained by Eqs. (11) and (13). Sequentially, the parameters a and b in Eq. (15) are determined by fitting the extracted cluster preformation factor P_c^{extr} in Eq. (20) within the experimental half-lives. Here, the parameter a remains the same for all the nuclei, while different values of parameter b are taken for the even-even (b_{e-e}) and odd-A (b_{o-A}) nuclei respectively to denote the various hindrance effects on cluster preformation factor, such as the blocking effect of the unpaired nucleon in odd-A nuclei and so on [14]. During the fitting procedure, the parameter a is determined together with b_{e-e} for even-even nuclei first. Then the parameter b_{o-A} for odd-A nuclei can be determined with the fixed parameter a.

As per Eqs. (7)–(9), both the theoretical quadrupole deformation parameter β_2^{theo} taken from FRDM2012 [40] and the experimental one β_2^{expt} [41] are used in our calculations for a contrast. Due to the lack of experimental data for the hexadecapole and hexacontatetrapole deformation parameters, only theoretical values β_4^{theo}, β_6^{theo} taken from FRDM2012 [40] are adopted in calculations. That is, two sets of deformation parameters (β_2^{theo}, β_4^{theo}, β_6^{theo}) and (β_2^{expt}, β_4^{theo}, β_6^{theo}) are respectively adopted in present work. It should be noticed here that the experimental value of β_2^{expt} has to be used together with the theoretical ones of β_4^{theo} and β_6^{theo} in the second parameter set, since the inclusion of hexadecapole and hexacontatetrapole deformation are found to be essential in calculating the half-lives of cluster radioactivity, especially for the cases with large quadrupole deformation (see the discussions in Sec. III B). Thus we give two sets of parameters a and b for the cases calculated with different deformation parameter sets. The optimized parameters a and b in Eq. (15) for cases calculated with (β_2^{theo}, β_4^{theo}, β_6^{theo}) are given together with the uncertainties as

$$a = -0.05663 \pm 0.00441,$$
$$b_{e-e} = 0.8501 \pm 0.6041,$$
$$b_{o-A} = -0.02201 \pm 0.18733, \qquad (21)$$

with the covariance matrix $\boldsymbol{\Sigma}_{e-e}$ for even-even nuclei and $\boldsymbol{\Sigma}_{o-A}$ for odd-A nuclei being

$$\boldsymbol{\Sigma}_{e-e} = \begin{bmatrix} \text{Cov}(a, a) & \text{Cov}(a, b_{e-e}) \\ \text{Cov}(b_{e-e}, a) & \text{Cov}(b_{e-e}, b_{e-e}) \end{bmatrix}$$
$$= \begin{bmatrix} 1.9434 \times 10^{-5} & -2.5889 \times 10^{-3} \\ -2.5889 \times 10^{-3} & 3.6502 \times 10^{-1} \end{bmatrix},$$

$$\boldsymbol{\Sigma}_{o-A} = \text{Cov}(b_{o-A}, b_{o-A}) = 3.5096 \times 10^{-2}. \qquad (22)$$
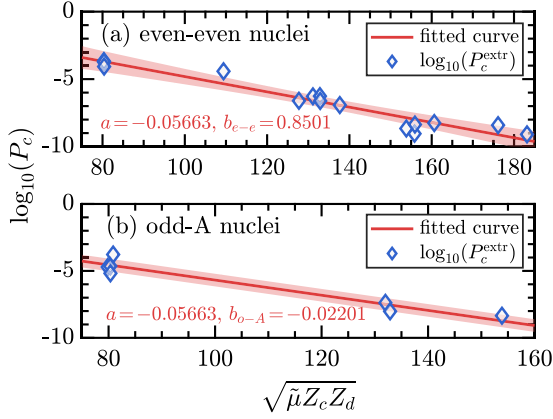
FIG. 2. The logarithm of cluster preformation factor $\log_{10}(P_c)$ extracted with deformation parameter set $(\beta_2^{\text{theo}}, \beta_4^{\text{theo}}, \beta_6^{\text{theo}})$ versus the quantity $\sqrt{\tilde{\mu} Z_c Z_d}$ for (a) even-even and (b) odd-A cluster emitters, respectively. Note that the linear fitted curves in red are to guide the eyes. The light red bands in both panels correspond to the 95% prediction intervals of the fitted curves.

Here, the matrix element $\text{Cov}(a, b)$ denotes the covariance between a and b. While for the cases calculated with $(\beta_2^{\text{expt}}, \beta_4^{\text{theo}}, \beta_6^{\text{theo}})$, the optimized parameters a and b are given as

$$a = -0.07892 \pm 0.00579,$$
$$b_{e-e} = 2.5932 \pm 0.7942,$$
$$b_{o-A} = 1.7829 \pm 0.1771, \tag{23}$$

with the covariance matrix being

$$\Sigma_{e-e} = \begin{bmatrix} 3.3584 \times 10^{-5} & -4.4739 \times 10^{-3} \\ -4.4739 \times 10^{-3} & 6.3078 \times 10^{-1} \end{bmatrix},$$
$$\Sigma_{o-A} = 3.1333 \times 10^{-2}. \tag{24}$$

The uncertainty of $\log_{10}(P_c)$ can be estimated by using the formula [52,53]

$$\sigma_{P_c}^2 = \sum_{i,j} \text{Cov}(x_i, x_j) \frac{\partial f}{\partial x_i} \frac{\partial f}{\partial x_j}, \tag{25}$$

in which f denotes the formula of Eq. (15), and x_i denotes the parameter a or b. For a clear insight, the logarithm of cluster preformation factor $\log_{10}(P_c^{\text{extr}})$ extracted with deformation parameter set $(\beta_2^{\text{theo}}, \beta_c^{\text{theo}}, \beta_6^{\text{theo}})$ and the analytical formula of Eq. (15) are presented in Fig. 2, where Fig. 2(a) represents even-even nuclei and Fig. 2(b) odd-A nuclei. The 95% prediction bands of the fitted curve are also presented. From Fig. 2, one can directly see the good linear dependence of $\log_{10}(P_c^{\text{extr}})$ on the quantity $\sqrt{\tilde{\mu} Z_c Z_d}$ in both panels, which shows a positive response to the assumption of cluster preformation factor in Eq. (15).

Within the above-mentioned deduced parameters, we give the theoretical results for the half-lives of cluster radioactivity by using the DDCM+ introduced in Sec. II A. Meanwhile, the theoretical half-lives obtained from the UDF introduced in Sec. II B are also given as contrasts. The detailed numerical results could be found in Table I. The first three columns present the serial numbers and detailed decay modes for

the various cluster emissions. Q_c denotes the decay energy, while l denotes the orbital angular momentum carried by the emitted cluster. β_2^{theo}, β_4^{theo}, and β_6^{theo} are separately the theoretical quadrupole, hexadecapole, and hexacontatetrapole deformation parameters for the emitted cluster mainly taken from Ref. [40], while β_2^{expt} is the experimental quadrupole deformation parameter taken from Ref. [41]. T_c^{expt} denotes the experimental half-lives of exotic heavy cluster radioactivity taken from Refs. [49,50]. T_c^{theo1} and T_c^{theo2} denote the theoretical half-lives of cluster radioactivity given by DDCM+ with $(\beta_2^{\text{theo}}, \beta_4^{\text{theo}}, \beta_6^{\text{theo}})$ and $(\beta_2^{\text{expt}}, \beta_4^{\text{theo}}, \beta_6^{\text{theo}})$, respectively, while T_c^{theo3} denotes the theoretical half-lives of cluster radioactivity given by UDF. Here, we adopt the same sign of β_2^{expt} with β_2^{theo}. For the heavy cluster-emitters with multiple decay channels, the values of T_c^{expt} listed in Table I are derived by $T_c^{\text{expt}} = T_{1/2}^{\text{expt}} / \gamma_c$ with $T_{1/2}^{\text{expt}}$ being the real experimental half-lives and γ_c being the corresponding branching ratios for the cluster radioactivity.

In Table I, we also present the uncertainties associated with the experimental and theoretical data, if available. The uncertainties of experimental quantities, such as Q_c, β_2^{expt}, and $\log_{10}(T_c^{\text{expt}})$, are extracted directly from the corresponding referenced sources of Refs. [41,49,50]. However, the uncertainties of theoretical deformation parameters $\beta_{2,4,6}^{\text{theo.}}$ are absent in Table I because they are not given in Ref. [40]. In addition, we give a preliminary and tentative estimation on the uncertainties of theoretical cluster radioactivity half-lives. This estimation is done by calculating the lower and upper bounds of theoretical half-lives, considering the uncertainties propagation of Q_c, β_2^{expt}, and $\log_{10}(P_c)$. It is evident in Table I that the theoretical uncertainties of $\log_{10}(T_c^{\text{theo2}})$ are relatively larger than those of $\log_{10}(T_c^{\text{theo1}})$, which is mainly attributed to the inclusion of uncertainties of β_2^{expt} in the calculations for $\log_{10}(T_c^{\text{theo2}})$. More accurate measurements of the deformation parameters could be anticipated to reduce the theoretical uncertainties significantly. Similarly, the theoretical uncertainties of $\log_{10}(T_c^{\text{theo3}})$ are the smallest among the three groups of theoretical half-lives, primarily because only the uncertainties of Q_c are considered in the calculations. The uncertainties propagation of the parameters for the UDF is not performed because the uncertainties of parameters are not available in the original source [14]. It is worth noting again that the current study is just a preliminary exploration of the uncertainties of the theoretical results. It is important to acknowledge that the total uncertainty of a theoretical model is usually known as a mixture of systematic, statistical, and experimental uncertainty [54]. Hence, a more accurate estimation of these uncertainties can be anticipated in the future through a more comprehensive and in-depth analysis.

One could see in Table I that both the theoretical results within the DDCM+ and UDF agree fairly well with the experimental data, despite the selected cluster radioactivities having extremely long half-lives in a wide range from 10^{11} to 10^{27} s. To see the agreement between the theoretical half-lives T_c^{theo} and the experimental data T_c^{expt} more intuitively, we plot the logarithmic deviations $\delta T = \log_{10}(T_c^{\text{theo}}/T_c^{\text{expt}})$ for the DDCM+ with $(\beta_2^{\text{theo}}, \beta_4^{\text{theo}}, \beta_6^{\text{theo}})$ and $(\beta_2^{\text{expt}}, \beta_4^{\text{theo}}, \beta_6^{\text{theo}})$, as well as UDF in Fig. 3, which are denoted by red

TABLE I. Calculations of the half-lives of exotic heavy cluster radioactivity in the trans-lead region, from ground state to ground state. In this table, Q_c denotes the decay energy, l is the angular momentum carried by the emitted cluster, β_2^{theo}, β_4^{theo}, and β_6^{theo} are separately the theoretical quadrupole, hexadecapole, and hexacontatetrapole deformation parameters for the emitted cluster mainly taken from Ref. [40], while β_2^{expt} is the experimental quadrupole deformation parameter taken from Ref. [41]. T_c^{expt} denotes the experimental half-lives of exotic heavy cluster radioactivity taken from Refs. [49,50]. T_c^{theo1} and T_c^{theo2} denote the theoretical half-lives of cluster radioactivity given by DDCM+ with $(\beta_2^{theo}, \beta_4^{theo}, \beta_6^{theo})$ and $(\beta_2^{expt}, \beta_4^{theo}, \beta_6^{theo})$, respectively, while T_c^{theo3} denotes the theoretical half-lives of cluster radioactivity given by UDF. All the half-lives are in units of seconds, the logarithms of which are presented for the sake of comparison. In this table, the experimental uncertainties are extracted from the corresponding referenced sources, in which the symbol "($\pm$?)" denotes the lack of uncertainty information for this datum. The lower and upper bounds of theoretical cluster radioactivity half-lives, resulting from the uncertainties of Q_c, β_2^{expt}, and P_c, are presented for useful references as well.

No.	Parent	Cluster	Q_c (MeV)	l	β_2^{theo}	β_4^{theo}	β_6^{theo}	β_2^{expt}	$\log_{10}(T_c^{expt})$	$\log_{10}(T_c^{theo1})$	$\log_{10}(T_c^{theo2})$	$\log_{10}(T_c^{theo3})$
1	^{221}Fr	^{14}C	$31.291^{+0.007}_{-0.007}$	3	-0.361^a	0.000	0.000	$-(0.361^{+0.024}_{-0.024})$	$14.515^{+0.058}_{-0.052}$	$14.347^{+0.201}_{-0.201}$	$14.322^{+0.226}_{-0.224}$	$14.625^{+0.014}_{-0.014}$
2	^{221}Ra	^{14}C	$32.396^{+0.005}_{-0.005}$	3	-0.361	0.000	0.000	$-(0.361^{+0.024}_{-0.024})$	$13.319^{+0.667}_{-0.319}$	$13.246^{+0.197}_{-0.197}$	$13.231^{+0.222}_{-0.223}$	$13.476^{+0.009}_{-0.009}$
3	^{222}Ra	^{14}C	$33.049^{+0.004}_{-0.004}$	0	-0.361	0.000	0.000	$-(0.361^{+0.024}_{-0.024})$	$11.049^{+0.181}_{-0.131}$	$11.089^{+0.281}_{-0.281}$	$11.136^{+0.401}_{-0.402}$	$11.022^{+0.007}_{-0.007}$
4	^{223}Ra	^{14}C	$31.828^{+0.003}_{-0.003}$	4	-0.361	0.000	0.000	$-(0.361^{+0.024}_{-0.024})$	$15.045^{+0.021}_{-0.019}$	$14.436^{+0.193}_{-0.193}$	$14.422^{+0.217}_{-0.219}$	$14.560^{+0.006}_{-0.006}$
5	^{224}Ra	^{14}C	$30.534^{+0.002}_{-0.002}$	0	-0.361	0.000	0.000	$-(0.361^{+0.024}_{-0.024})$	$15.895^{+0.155}_{-0.114}$	$15.856^{+0.279}_{-0.278}$	$15.903^{+0.399}_{-0.401}$	$15.864^{+0.004}_{-0.004}$
6	^{225}Ac	^{14}C	$30.476^{+0.007}_{-0.007}$	4	-0.361	0.000	0.000	$-(0.361^{+0.024}_{-0.024})$	$17.279^{+0.162}_{-0.118}$	$18.104^{+0.202}_{-0.202}$	$18.102^{+0.228}_{-0.229}$	$18.237^{+0.014}_{-0.014}$
7	^{226}Ra	^{14}C	$28.197^{+0.003}_{-0.003}$	0	-0.361	0.000	0.000	$-(0.361^{+0.024}_{-0.024})$	$21.288^{+0.116}_{-0.092}$	$20.919^{+0.281}_{-0.278}$	$20.968^{+0.401}_{-0.402}$	$20.937^{+0.007}_{-0.007}$
8	^{228}Th	^{20}O	$44.723^{+0.002}_{-0.002}$	0	0.010	-0.024	0.020	$0.269^{+0.011}_{-0.008}$	$20.728^{+0.058}_{-0.077}$	$21.650^{+0.181}_{-0.181}$	$21.773^{+0.269}_{-0.278}$	$21.539^{+0.004}_{-0.004}$
9	^{230}U	^{22}Ne	$61.388^{+0.005}_{-0.005}$	0	0.384	0.096	-0.007	$0.562^{+0.005}_{-0.005}$	$19.561^{+0.235}_{-0.152}$	$19.339^{+0.152}_{-0.151}$	$19.061^{+0.237}_{-0.237}$	$20.091^{+0.007}_{-0.007}$
10	^{230}Th	^{24}Ne	$57.760^{+0.021}_{-0.021}$	0	-0.063	0.013	-0.030	$-(0.418^{+0.084}_{-0.035})$	$24.613^{+0.112}_{-0.091}$	$24.910^{+0.173}_{-0.176}$	$25.070^{+0.346}_{-0.533}$	$24.580^{+0.033}_{-0.033}$
11	^{231}Pa	^{24}Ne	$60.410^{+0.005}_{-0.005}$	1	-0.063	0.013	-0.030	$-(0.418^{+0.084}_{-0.035})$	$22.886^{+0.062}_{-0.055}$	$22.996^{+0.196}_{-0.196}$	$23.117^{+0.312}_{-0.498}$	$23.086^{+0.008}_{-0.008}$
12	^{232}U	^{24}Ne	$62.310^{+0.002}_{-0.002}$	0	-0.063	0.013	-0.030	$-(0.418^{+0.084}_{-0.035})$	$20.388^{+0.038}_{-0.035}$	$20.799^{+0.145}_{-0.145}$	$21.002^{+0.316}_{-0.503}$	$20.356^{+0.003}_{-0.003}$
13	^{233}U	^{24}Ne	$60.485^{+0.003}_{-0.003}$	2	-0.063	0.013	-0.030	$-(0.418^{+0.084}_{-0.035})$	$24.844^{+0.058}_{-0.052}$	$24.369^{+0.191}_{-0.192}$	$24.502^{+0.309}_{-0.497}$	$24.412^{+0.005}_{-0.005}$
14	^{234}U	^{24}Ne	$58.825^{+0.002}_{-0.002}$	0	-0.063	0.013	-0.030	$-(0.418^{+0.084}_{-0.035})$	$25.935^{+0.654}_{-0.251}$	$25.991^{+0.146}_{-0.144}$	$26.179^{+0.318}_{-0.507}$	$25.811^{+0.003}_{-0.003}$
15	^{234}U	^{26}Ne	$59.413^{+0.018}_{-0.018}$	0	0.121	-0.052	-0.035	$0.413^{+0.043}_{-0.043}$	$25.935^{+0.654}_{-0.251}$	$25.958^{+0.172}_{-0.173}$	$25.602^{+0.525}_{-0.537}$	$26.520^{+0.031}_{-0.031}$
16	^{234}U	^{28}Mg	$74.111^{+0.021}_{-0.021}$	0	0.277	-0.073	0.008	$0.503^{+0.031}_{-0.031}$	$25.540^{+0.339}_{-0.342}$	$24.743^{+0.198}_{-0.195}$	$24.610^{+0.526}_{-0.534}$	$25.255^{+0.029}_{-0.029}$
17	^{235}U	^{28}Mg	$72.426^{+0.031}_{-0.031}$	1	0.277	-0.073	0.008	$0.503^{+0.031}_{-0.031}$	27.444 ($\pm$?)	$27.832^{+0.233}_{-0.227}$	$27.632^{+0.498}_{-0.505}$	$29.002^{+0.045}_{-0.045}$
18	^{236}Pu	^{28}Mg	$79.670^{+0.002}_{-0.002}$	0	0.277	-0.073	0.008	$0.503^{+0.031}_{-0.031}$	$21.524^{+0.102}_{-0.133}$	$20.456^{+0.177}_{-0.175}$	$20.357^{+0.511}_{-0.521}$	$20.763^{+0.003}_{-0.003}$
19	^{238}Pu	^{28}Mg	$75.912^{+0.002}_{-0.002}$	0	0.277	-0.073	0.008	$0.503^{+0.031}_{-0.031}$	25.664 ($\pm$?)	$25.276^{+0.176}_{-0.176}$	$25.162^{+0.512}_{-0.519}$	$25.962^{+0.003}_{-0.003}$
20	^{238}Pu	^{30}Mg	$76.793^{+0.002}_{-0.002}$	0	0.119	-0.005	-0.031	$0.415^{+0.021}_{-0.021}$	25.664 ($\pm$?)	$25.654^{+0.191}_{-0.191}$	$25.079^{+0.446}_{-0.451}$	$26.104^{+0.003}_{-0.003}$
21	^{238}Pu	^{32}Si	$91.187^{+0.021}_{-0.021}$	0	-0.124	-0.030	-0.033	$-(0.228^{+0.034}_{-0.021})$	25.296 ($\pm$?)	$26.008^{+0.262}_{-0.262}$	$26.289^{+0.422}_{-0.489}$	$25.588^{+0.026}_{-0.026}$
22	^{242}Cm	^{34}Si	$96.544^{+0.002}_{-0.002}$	0	0.000	0.000	-0.039	$0.183^{+0.035}_{-0.035}$	$23.107^{+0.197}_{-0.135}$	$23.534^{+0.262}_{-0.264}$	$23.979^{+0.633}_{-0.667}$	$23.481^{+0.003}_{-0.003}$

^{a}The value and sign of quadrupole deformation parameter for ^{14}C are separately taken from Refs. [41] and [51].

circles, green squares, and blue diamonds in Figs. 3(a)–3(c), respectively. Running horizontally along Fig. 3 is the serial number of various cluster radioactivities, which is listed in the first column of Table I. The black dot-dashed lines correspond to the deviations within a factor of ten. As shown in Fig. 3, the δT values for the most of nuclei are found to lie between the two black lines, implying that the theoretical results are in reasonable agreement with the latest experimental data. Nevertheless, the relatively larger deviations can be seen for several cluster radioactivities, such as ^{228}Th $\rightarrow$ ^{208}Pb + ^{20}O and ^{236}Pu $\rightarrow$ ^{208}Pb + ^{28}Mg. This may indicate that more structural factors, e.g., nuclear surface polarization and so on, should be considered in the calculations, which we shall discuss in Sec. III B soon. In addition, the measuring error may also result in large deviations between the theoretical results and experimental data. For example, ^{20}O emission of ^{228}Th has a tiny branching ratio of $1.13^{+0.22}_{-0.22} \times 10^{-13}$, which is even much smaller than the one measured for ^{14}C emission of ^{223}Ra ($8.9^{+0.4}_{-0.4} \times 10^{-10}$) [49]. In the original literature for

^{20}O emission of ^{228}Th [55], the authors introduced the "rarity" of ^{20}O emission from ^{228}Th, and also mentioned that several so-different theories had reproduced its experimental half-life within a factor of ten as well. Consequently, the results may be improved with more accurate experimental data in the future.

Finally, to systematically evaluate the agreements between the theoretical half-lives and experimental data, we also calculate the root-mean-square (rms) deviations between theoretical and experimental half-lives of $\sigma = \{\frac{1}{\mathcal{N}} \sum_{i=1}^{\mathcal{N}} [\log_{10}(T_c^{theo, i}/T_c^{expt, i})]^2\}^{1/2}$, with i denoting the ith nuclei, and $\mathcal{N}$ being the total number of nuclei included in present calculations. As shown in Fig. 3, the rms deviation for the DDCM+ with $(\beta_2^{expt}, \beta_4^{theo}, \beta_6^{theo})$ and $(\beta_2^{expt}, \beta_4^{theo}, \beta_6^{theo})$, as well as UDF are 0.4954, 0.6068, and 0.5412, respectively. All of these theoretical results agree well with the experimental data. Furthermore, the rms deviation for the DDCM+ with $(\beta_2^{expt}, \beta_4^{theo}, \beta_6^{theo})$ is found to be slightly larger than that of the other two cases, which may due to the lack of experimental values of hexadecapole and hexacontatetrapole deformation
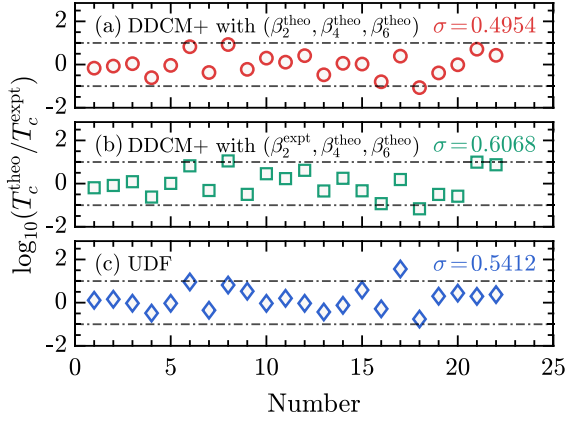
FIG. 3. The logarithmic deviations between the experimental data and the theoretical results given by (a) DDCM+ with (β_2^{theo}, β_4^{theo}, β_6^{theo}), (b) DDCM+ with (β_2^{expt}, β_4^{theo}, β_6^{theo}), and (c) the UDF. The black dot-dashed lines in each panel correspond to the deviation between the theoretical results and the experimental data with a factor of ten.

parameters. Moreover, β_2^{expt} may not be self-consistent with β_4^{theo} and β_6^{theo} as well. One can see that the value of β_2^{expt} in Table I varies in a very large range from -0.418 to 0.562, then the hexadecapole and hexacontatetrapole deformation would play important roles in calculating half-lives of cluster radioactivity and should not be negligible. Thus, more abundant experimental data of nuclear hexadecapole and hexacontatetrapole deformation are anticipated to improve the results. The above theoretical results demonstrate that the DDCM+ is a reliable model in the studies of cluster-radioactivity half-lives.

B. Effects of nuclear surface polarization on exotic cluster radioactivity

In view of the good reliability of the DDCM+ shown in Sec. III A, we tend to discuss the effects of nuclear surface polarization on the cluster radioactivity within DDCM+ in this section. The theoretical deformation parameter set (β_2^{theo}, β_4^{theo}, β_6^{theo}) would be used in calculations hereafter. Denoting, by a_L^τ and a_S^τ the diffuseness along the elongated and compressed axis, then we can define the different polarization modes of one deformed nucleus via the quantity $\delta a = (a_L^\tau - a_S^\tau)/a_0^\tau$. According to the values of δa, one can find that there may be three different polarization modes as follows:

(i) When $\delta a < 0$, the surface diffuseness of a deformed system tends to reduce along the elongated axis while increasing along the compressed axis. This is just an approximate of the case proposed in Ref. [35] for a deformed heavy nucleus, which is denoted "mode 1" in the present work.

(ii) When $\delta a = 0$, there is no diffuseness polarization occurring along the two symmetric axes. The surface diffuseness would be identical to the corresponding spherical case along both the elongated and compressed axis, while anisotropic at the other orientation angles. This is denoted "mode 2" in the present work,

which corresponds to the case proposed by Bohr and Mottelson [34].

(iii) When $\delta a > 0$, it is on the opposite side of case 1 that the surface diffuseness of a deformed system would increase along the elongated axis while reducing along the compressed axis. This is denoted "mode 3" in the present work, which is similar to the case utilized in Ref. [11].

In terms of Ref. [35], the surface polarization of mode 1 holds true for the most of deformed heavy nuclei with $A > 120$. While a systematic tendency of the surface polarization in the light system is difficult to discover, all three cases introduced above are plausible (see Figs. 4 and 10 of Ref. [35] for more details). Through the detailed comparison of the theoretical results with the above three polarization modes, the effects of different surface polarization modes on the exotic cluster radioactivities could be well investigated. Hereafter, we shall take the cluster radioactivity $^{236}\text{Pu} \rightarrow {}^{208}\text{Pb} + {}^{28}\text{Mg}$ for illustration, involving a spherical daughter nucleus ^{208}Pb interacting with a deformed cluster ^{28}Mg.

For sake of intuitive illustration, we take $k' = -1$, 0, and 1 in Eq. (9) to denote mode 1, 2, and 3, respectively. Then we show the form factor of half-density radius $f_\mathcal{R}(\theta) = \mathcal{R}^\tau(\theta)/\mathcal{R}_0^\tau$ and diffuseness $f_a^{k'}(\theta) = a^\tau(k', \theta)/a_0^\tau$ for ^{28}Mg in Fig. 4(a). In Fig. 4(a), the values of $f_\mathcal{R}(\theta)$ are denoted by black circles, while the values of $f_a^{k'}(\theta)$ with $k' = -1$, 0, and 1 are denoted by red diamonds, blue triangles, and green squares, respectively. According to Fig. 4(a), the elongated axis for ^{28}Mg goes along with the angle $\theta = 0$ while the compressed axis goes along with the angle $\theta = \pi/2$. The diffuseness becomes anisotropic in all three polarization modes due to deformation, and the behavior of diffuseness varies with the changing of parameter k' at the angle $\theta = 0$ and $\theta = \pi/2$, which is consistent with the descriptions of modes 1–3. Further investigation reveals that the sign of parameter k' determines the specific polarization mode of the emitted cluster, with $k' < 0$ corresponding to mode 1, $k' = 0$ corresponding to mode 2, and $k' > 0$ corresponding to mode 3 (strictly speaking, this relationship is not always established for all the deformed system, but it holds for all the emitted cluster considered in present work). In Fig. 4(b), a linear correlation between the quantity δa and parameter k' can be directly observed, with the slope calculated as $\frac{3}{4}\sqrt{\frac{5}{\pi}}|\beta_2| = 0.2621$ according to Eq. (9). This means that the amplitude of k' handles the degree of surface polarization for a deformed nucleus.

To figure out the sensitivity of cluster-daughter interaction to the different polarization modes, we illustrate in Figs. 5(a) and 5(b) the sum of nuclear and Coulomb potential near the barrier region for the $^{208}\text{Pb} \otimes {}^{28}\text{Mg}$ system. Similar to Fig. 4, we also take the specific values of $k' = -1$, 0, and 1 to represent modes 1–3 and plot the daughter-cluster interaction in various cases. Due to the deformation of ^{28}Mg, the daughter-cluster interaction is anisotropic at different orientation angles ξ. The barrier height at $\xi = 0°$ is obviously lower than at $\xi = 90°$. In addition, differing polarization modes may alter the geometry of interactions as well. In Fig. 5(c), we further
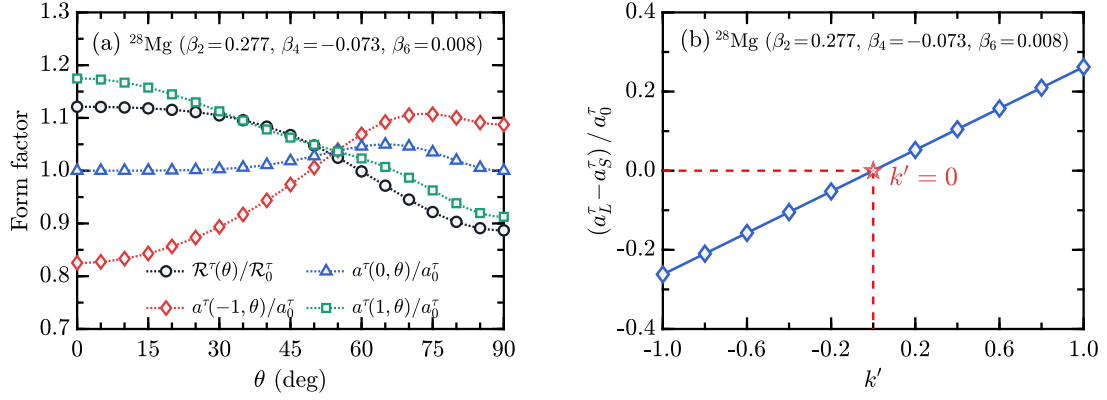
FIG. 4. (a) The form factor of half-density radius $f_{\mathcal{R}}(\theta) = \mathcal{R}^{\tau}(\theta)/\mathcal{R}_0^{\tau}$ and diffuseness $f_a^{k'}(\theta) = a^{\tau}(k',\theta)/a_0^{\tau}$ with $k' = -1, 0$, and 1 versus the angle θ for ^{28}Mg. (b) The quantity $\delta a = (a_L^{\tau} - a_S^{\tau})/a_0^{\tau}$ for ^{28}Mg as a function of parameter k' ranging in $-1 \leqslant k' \leqslant 1$.

present the variations of potential barrier height $V_B(\xi)$ and the logarithmic partial decay width $\log_{10}[\Gamma(\xi)]$ in Eq. (11) with the orientation angle ξ for the cluster radioactivity ^{236}Pu $\rightarrow$ ^{208}Pb $+ ^{28}$Mg. As shown, both the barrier height and partial decay width are anisotropic along different orientations, and a higher potential barrier would yield a smaller decay width. For example, the barrier heights at $\xi = 0°$ are 117.017, 115.780, and 114.376 MeV for mode 1, 2, and 3, respectively, the values of which increase to 118.861, 119.446, and 119.954 MeV at $\xi = 90°$. As for the partial decay width (in MeV), the logarithmic values at $\xi = 0°$ are -33.555, -32.896, and -32.118 for modes 1, 2, and 3, respectively, whereas reducing to -35.420, -35.672, and -35.880 at $\xi = 90°$. This can be easily understood by the quantum tunneling theory. It is well established that the penetration probability of the cluster is particularly sensitive to the height of inner potential barrier, which decreases exponentially as the barrier height increases. Therefore, according to Eqs. (13) and (14), the varied polarization modes would certainly lead to a considerable variation in the half-life of cluster radioactivity, which we will discuss next.

To manifest the overall impacts of different surface polarization modes on the cluster radioactivity half-life, we define the percentage change $\mathcal{D}_{k'}$ in the half-life for a cluster

emission as

$$\mathcal{D}_{k'} = \frac{T_c^{k'} - T_c^0}{T_c^0} \times 100\%, \tag{26}$$

in which $T_c^{k'}$ denotes the theoretical half-life of cluster radioactivity in one specific k' value and T_c^0 denotes that in spherical case (namely, $\beta_2 = \beta_4 = \beta_6 = 0$). Here we still take the cluster radioactivity ^{236}Pu $\rightarrow$ ^{208}Pb $+ ^{28}$Mg as an example, and proceed to show in Fig. 6 the variation of $\mathcal{D}_{k'}$ values with changing k' in a range of $-1 \leqslant k' \leqslant 1$. The red star in Fig. 6 represents mode 2 with $k' = 0$. Several interesting features emerge from Fig. 6:

(i) All the $\mathcal{D}_{k'}$ values presented in this figure are negative, indicating that the deformation would shorten the theoretical half-life of cluster radioactivity ^{236}Pu $\rightarrow$ ^{208}Pb $+ ^{28}$Mg regardless of the surface polarization mode. This is consistent with the previous researches [11,25].

(ii) In contrast to mode 2 with $k' = 0$, mode 1 with $k' < 0$ yields longer theoretical half-lives, whereas mode 3 with $k' > 0$ yields shorter theoretical half-lives as the amplitude of k' grows.
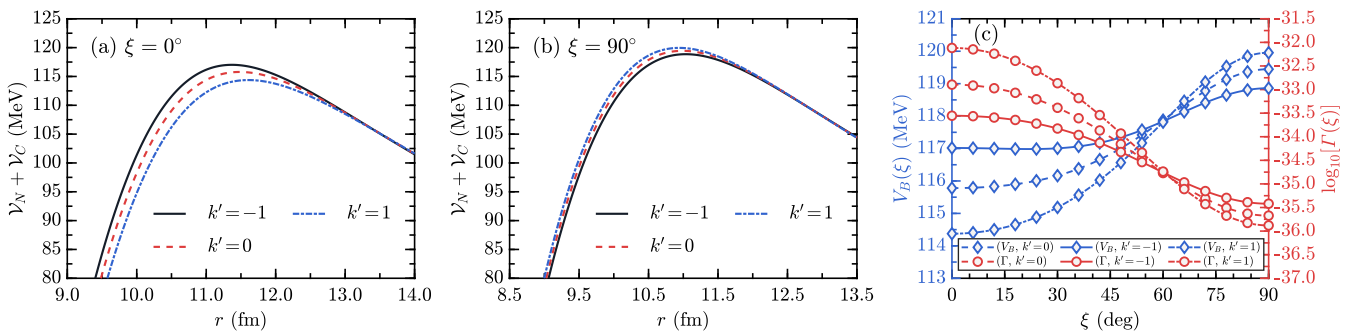

FIG. 5. Impact on the cluster-daughter potential due to different polarization modes at orientation angle (a) $\xi = 0$ and (b) $\xi = \pi/2$, as well as (c) the potential barrier height $V_B(\xi)$ and the logarithm of partial decay width $\log_{10}[\Gamma(\xi)]$ varying with the orientation angle ξ for the cluster radioactivity ^{236}Pu $\rightarrow$ ^{208}Pb $+ ^{28}$Mg. In panels [(a)–(c)], the solid, dashed, and dot-dashed lines respectively denote the cases with $k' = -1$, $k' = 0$, and $k' = 1$. Specially, the diamonds represent the potential barrier height while the circles denote the logarithmic partial decay width in panel (c). In addition, only the barrier regions are plotted in panels (a) and (b) for clarity.
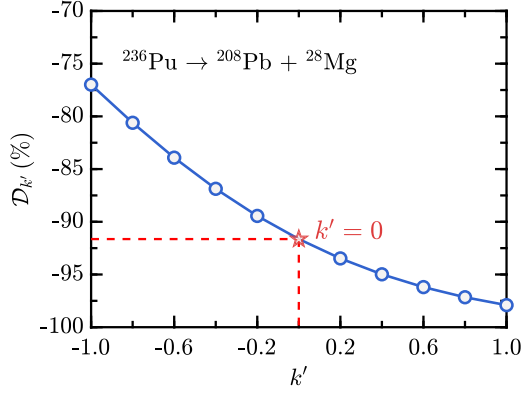
FIG. 6. The percentage change $\mathcal{D}_{k'}$ in the half-life varies with the change of parameter k' for the cluster radioactivity ^{236}Pu $\rightarrow$ ^{208}Pb + ^{28}Mg. The red star represents the $\mathcal{D}_{k'}$ value of mode two with $k' = 0$.

(iii) The changing rate of $\mathcal{D}_{k'}$ values with parameter k' gradually decreases as k' grows, and it is noticeably larger in mode 1 with $k' < 0$ than in mode 3 with $k' > 0$, indicating the theoretical half-life in mode 1 is more sensitive to the changes in the amplitude of k' than mode 3 for the cluster radioactivity ^{236}Pu $\rightarrow$ ^{208}Pb + ^{28}Mg.

Denoting $\mathcal{D}_{k'}^{-1}$, $\mathcal{D}_{k'}^{0}$, and $\mathcal{D}_{k'}^{1}$ by the values of $\mathcal{D}_{k'}$ with $k' = -1, 0$, and 1 for all the cluster radioactivities in Table I,

we further present these values in the last three columns of Table II. Meanwhile, the logarithm of half-lives for various cluster radioactivities in spherical cases assuming $P_c = 1$ are also given as $\log_{10}(T_c^0)$ in Table II for reference. From Table II, we can see that all the $\mathcal{D}_{k'}$ values are negative, indicating the first conclusion deduced from Fig. 6 is also well established for other cluster radioactivities, i.e., the half-lives would decrease after the inclusion of deformation regardless of the surface polarization mode. Moreover, the second feature mentioned above holds true for all the cluster radioactivities as well. However, the third conclusion deduced from Fig. 6 is not always established for all the cluster radioactivities. For example, the differences between $\mathcal{D}_{k'}^{-1}$ and $\mathcal{D}_{k'}^{0}$ for the ^{28}Mg emissions are significantly greater than that between $\mathcal{D}_{k'}^{1}$ and $\mathcal{D}_{k'}^{0}$, whereas the differences are almost the same for ^{32,34}Si emissions. This may be due to the different values of the deformation parameters. Therefore, in the end, we continue to check the sensitivity of the theoretical half-life with the changes of deformation parameters. Here we mainly consider the quadrupole β_2 and hexadecapole β_4 deformation parameters. We plot in Fig. 7 the logarithmic derivations between the theoretical half-life given by DDCM+ and that of spherical case for ^{236}Pu $\rightarrow$ ^{208}Pb + ^{28}Mg, denoted as $\log_{10}(T_c^\beta/T_c^0)$, versus the deformation parameters β_2 and β_4 in ranges of $-0.3 \leqslant \beta_2 \leqslant 0.3$ and $-0.1 \leqslant \beta_4 \leqslant 0.1$. The cases with $k' = -1$ and $k' = 1$ are respectively displayed in panels (a) and (b) of Fig. 7. From both Figs. 7(a) and 7(b), one could see that the half-life would decrease with the growth of $|\beta_2|$ regardless
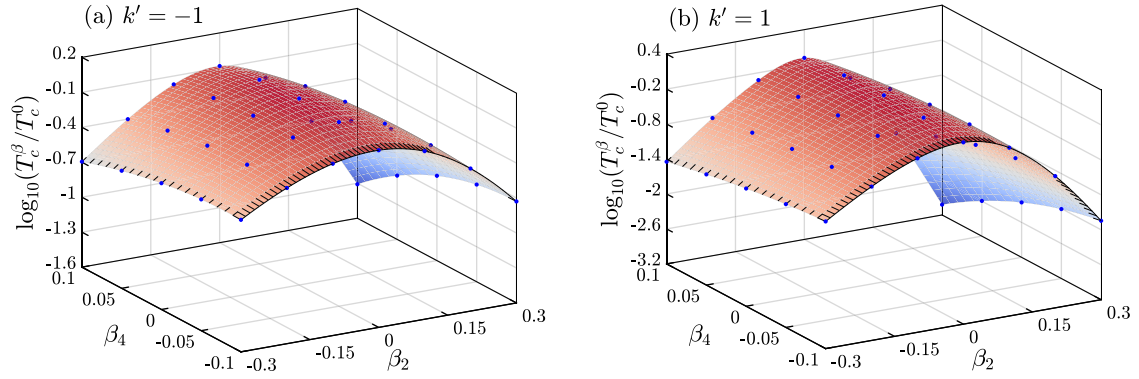
TABLE II. Percent changes $\mathcal{D}_{k'}(\%)$ of cluster radioactivity half-lives for different surface polarization modes. β_2^{theo}, β_4^{theo}, and β_6^{theo} are separately the theoretical quadrupole, hexadecapole, and hexacontatetrapole deformation parameters for the emitted cluster mainly taken from Ref. [40]. T_c^0 denotes the half-lives of cluster radioactivity in spherical cases assuming $P_c = 1$, which are in units of seconds. The last three columns display the values of $\mathcal{D}_{k'}$ for various cluster radioactivities in mode 1 with $k' = -1$, mode 2 with $k' = 0$ and mode 3 with $k' = 1$, respectively.

No.	Parent	Daughter	Cluster	β_2^{theo}	β_4^{theo}	β_6^{theo}	$\log_{10}(T_c^0)$	$\mathcal{D}_{k'}^{-1}(\%)$	$\mathcal{D}_{k'}^{0}(\%)$	$\mathcal{D}_{k'}^{1}(\%)$
1	^{221}Fr	^{207}Tl	^{14}C	-0.361[a]	0.000	0.000	10.128	-32.911	-52.340	-72.744
2	^{221}Ra	^{207}Pb	^{14}C	-0.361	0.000	0.000	8.999	-32.953	-52.380	-72.791
3	^{222}Ra	^{208}Pb	^{14}C	-0.361	0.000	0.000	7.709	-32.619	-51.835	-72.241
4	^{223}Ra	^{209}Pb	^{14}C	-0.361	0.000	0.000	10.188	-32.984	-52.376	-72.690
5	^{224}Ra	^{210}Pb	^{14}C	-0.361	0.000	0.000	12.480	-33.078	-52.510	-72.777
6	^{225}Ac	^{211}Bi	^{14}C	-0.361	0.000	0.000	13.625	-33.474	-53.127	-73.378
7	^{226}Ra	^{212}Pb	^{14}C	-0.361	0.000	0.000	17.549	-33.485	-53.110	-73.256
8	^{228}Th	^{208}Pb	^{20}O	0.010	-0.024	0.020	16.313	-1.588	-1.663	-1.784
9	^{230}U	^{208}Pb	^{22}Ne	0.384	0.096	-0.007	14.832	-91.600	-98.668	-99.882
10	^{230}Th	^{206}Hg	^{24}Ne	-0.063	0.013	-0.030	18.388	-7.463	-11.613	-17.030
11	^{231}Pa	^{207}Tl	^{24}Ne	-0.063	0.013	-0.030	15.553	-7.425	-11.583	-17.026
12	^{232}U	^{208}Pb	^{24}Ne	-0.063	0.013	-0.030	14.181	-7.407	-11.541	-16.954
13	^{233}U	^{209}Pb	^{24}Ne	-0.063	0.013	-0.030	16.877	-7.498	-11.664	-17.097
14	^{234}U	^{210}Pb	^{24}Ne	-0.063	0.013	-0.030	19.370	-7.567	-11.755	-17.201
15	^{234}U	^{208}Pb	^{26}Ne	0.121	-0.052	-0.035	19.256	-28.709	-42.951	-58.380
16	^{234}U	^{206}Hg	^{28}Mg	0.277	-0.073	0.008	17.966	-77.426	-91.756	-97.904
17	^{235}U	^{207}Hg	^{28}Mg	0.277	-0.073	0.008	20.194	-77.864	-91.973	-97.968
18	^{236}Pu	^{208}Pb	^{28}Mg	0.277	-0.073	0.008	13.559	-76.987	-91.628	-97.906
19	^{238}Pu	^{210}Pb	^{28}Mg	0.277	-0.073	0.008	18.397	-78.049	-92.070	-98.005
20	^{238}Pu	^{208}Pb	^{30}Mg	0.119	-0.005	-0.031	17.723	-34.403	-51.640	-67.952
21	^{238}Pu	^{206}Hg	^{32}Si	-0.124	-0.030	-0.033	17.128	-30.303	-42.988	-55.839
22	^{242}Cm	^{208}Pb	^{34}Si	0.000	0.000	-0.039	14.035	-5.025	-5.025	-5.025

[a]The value and sign of quadrupole deformation parameter for ^{14}C are separately taken from Refs. [41] and [51].

FIG. 7. The logarithmic derivations between the theoretical half-life given by DDCM+ and that of spherical case (denoted by T_c^0) with (a) $k' = -1$ and (b) $k' = 1$, as a function of deformation parameters β_2 and β_4 of ^{28}Mg in the emission of ^{236}Pu.

of the sign of β_2 when the value of β_4 is fixed, and the decreasing rate of the half-life with the quadrupole deformation parameter β_2 is slightly smaller in the oblate shape ($\beta_2 < 0$) of the cluster than in the prolate case ($\beta_2 > 0$). When the value of β_2 is fixed, the half-life is found to decrease as the value of β_4 grows from -0.1 to 0.1. It is also interesting to see that the decreasing trend of the half-life with β_4 is much more evident in the prolate cases. While in the oblate cases, the half-life decreases relatively slower with the growth of β_4 than that in the prolate cases. Moreover, it can be directly seen that the half-life would decrease much more drastically with the growth of β_4 when the cluster has a larger quadrupole deformation in both cases. For instance, as shown in Fig. 7(b), when $\beta_2 = 0$, the value of $\log_{10}(T_c^\beta/T_c^0)$ reduces by 0.083 with β_4 varying from 0 to 0.1. When $\beta_2 = 0.300$, however, the value of $\log_{10}(T_c^\beta/T_c^0)$ reduces by 0.765 with β_4 varying from 0 to 0.1, which means the effects of higher multipole deformation are not negligible in calculating half-lives of cluster radioactivity and should be considered in the calculations especially for the cases with large quadrupole deformation.

As a result, all of these discussed above indicate that the deformation would determine the obviousness of the surface polarization effects on cluster radioactivity half-lives, together with the amplitude of parameter k'. This is also consistent with the conclusions obtained from our previous studies on α decay [28,29].

IV. SUMMARY AND CONCLUSIONS

In summary, we systematically investigate the effect of nuclear surface polarization on the exotic cluster radioactivity via DDCM+. Especially, three different surface polarization modes for the emitted cluster are taken into account by introducing an adjustable parameter k' into the deformation-dependent diffuseness parameter, the value of which handles the specific mode and degree of the nuclear surface polarization. In this work, we first examine the capability of DDCM+ in studying exotic cluster radioactivity with temporarily taking $k' = 0$. A total of 22 cluster emissions with certain half-lives and branching ratios are selected in our calculations. The theoretical results given by DDCM+ are in good accordance with the latest experimental data within

a factor of ≈ 3, indicating DDCM+ is reliable for studying exotic cluster radioactivity.

Sequentially, we investigate the effect of surface polarization on cluster radioactivity half-lives by considering three different polarization modes with mode 1–3. It is found that the surface polarization would change the geometry of daughter-cluster interaction and optimize the half-life of cluster radioactivity accordingly. The global conclusions are summarized as follows:

(i) Including the effects of deformation of the light cluster in cluster radioactivity would lead to a decrease of half-life regardless of the nuclear surface polarization mode.

(ii) Different surface polarization modes of nuclei would have various effects on the half-life of cluster radioactivity. Concretely, in contrast to the case of mode 2 with $k' = 0$ which has no polarization along both symmetric axes, the surface polarization of mode 1 with $k' < 0$ lengthens the theoretical half-lives, whereas the surface polarization of mode 3 with $k' > 0$ shortens the theoretical half-lives as the amplitude of k' grows.

(iii) Except for the amplitude of parameter k', the obviousness of the surface polarization effects also depends on the deformation degree of the emitted cluster. It would be much more evident for the diffuseness polarization effects on the half-life of cluster radioactivity as the emitted cluster has a larger deformation degree.

The present work makes a detailed analysis of the possible surface diffuseness polarization effects on the half-life of cluster radioactivity, it is expected that these results could be useful for the forthcoming experimental and theoretical studies on nuclear structure. Furthermore, the experimental confirmation and explanation of the nuclear surface polarization phenomenon are also anticipated in the future.

[1] S. A. Giuliani, Z. Matheson, W. Nazarewicz, E. Olsen, P. G. Reinhard, J. Sadhukhan, B. Schuetrumpf, N. Schunck, and P. Schwerdtfeger, Rev. Mod. Phys. **91**, 011001 (2019).

[2] A. Săndulescu, D. N. Poenaru, and W. Greiner, Sov. J. Part. Nucl. **11**, 528 (1980).

[3] H. J. Rose and G. A. Jones, Nature (London) **307**, 245 (1984).

[4] S. W. Barwick, P. B. Price, and J. D. Stevenson, Phys. Rev. C **31**, 1984 (1985).

[5] R. Bonetti, C. Carbonini, A. Guglielmetti, M. Hussonnois, D. Trubert and C. Le Naour, Nucl. Phys. A **686**, 64 (2001).

[6] G. Royer and R. Moustabchir, Nucl. Phys. A **683**, 182 (2001).

[7] Z. Ren, C. Xu, and Z. Wang, Phys. Rev. C **70**, 034304 (2004).

[8] D. Ni, Z. Ren, T. Dong, and C. Xu, Phys. Rev. C **78**, 044310 (2008).

[9] Y. Qian, Z. Ren, and D. Ni, Phys. Rev. C **94**, 024315 (2016).

[10] V. Y. Denisov, Phys. Rev. C **88**, 044608 (2013).

[11] D. F. Rojas-Gamboa, J. E. P. Velasquez, N. G. Kelkar, and N. J. Upadhyay, Phys. Rev. C **105**, 034311 (2022).

[12] L. J. Qi, D. M. Zhang, S. Luo, X. H. Li, X. J. Wu, and C. T. Liang, Chin. Phys. C **47**, 014101 (2023).

[13] M. Ismail and A. Adel, J. Phys. G **49**, 075102 (2022).

[14] D. Ni and Z. Ren, Phys. Rev. C **82**, 024311 (2010).

[15] W. M. Seif, A. R. Abdulghany, and Z. N. Hussein, J. Phys. G **48**, 025111 (2021).

[16] D. N. Poenaru, R. A. Gherghescu, and W. Greiner, Phys. Rev. Lett. **107**, 062503 (2011).

[17] X. J. Bao, H. F. Zhang, B. S. Hu, G. Royer, and J. Q. Li, J. Phys. G **39**, 095103 (2012).

[18] K. P. Santhosh and T. A. Jose, Phys. Rev. C **99**, 064604 (2019).

[19] G. Royer, Q. Ferrier, and M. Pineau, Nucl. Phys. A **1021**, 122427 (2022).

[20] C. Qi, F. R. Xu, R. J. Liotta, and R. Wyss, Phys. Rev. Lett. **103**, 072501 (2009).

[21] D. N. Poenaru, R. A. Gherghescu, and W. Greiner, Phys. Rev. C **83**, 014601 (2011).

[22] Y. L. Zhang and Y. Z. Wang, Phys. Rev. C **97**, 014318 (2018).

[23] S. Cheng, W. Wu, L. Cao, and F. S. Zhang, Eur. Phys. J. A **58**, 168 (2022).

[24] C. Xu and Z. Ren, Nucl. Phys. A **753**, 174 (2005).

[25] C. Xu and Z. Ren, Phys. Rev. C **74**, 014304 (2006).

[26] D. Bai and Z. Ren, Eur. Phys. J. A **54**, 220 (2018).

[27] D. Bai and Z. Ren, Phys. Rev. C **103**, 044316 (2021).

[28] Z. Wang and Z. Ren, Phys. Rev. C **106**, 024311 (2022).

[29] Z. Wang, D. Bai, and Z. Ren, Phys. Rev. C **105**, 024327 (2022).

[30] Y. Qian and Z. Ren, Sci. China: Phys. Mech. Astron. **56**, 1520 (2013).

[31] Y. Qian and Z. Ren, Eur. Phys. J. A **52**, 68 (2016).

[32] Z. Yuan, D. Bai, Z. Wang, Z. Ren, and D. Ni, Sci. China: Phys. Mech. Astron. **66**, 222012 (2023).

[33] L. Zhou, S. M. Wang, D. Q. Fang, and Y. G. Ma, Nucl. Sci. Tech. **33**, 105 (2022).

[34] A. Bohr and B. Mottelson, *Nuclear Structure Vol. 2: Nuclear Deformations* (World Scientific, Singapore, 1998).

[35] G. Scamps, D. Lacroix, G. G. Adamian, and N. V. Antonenko, Phys. Rev. C **88**, 064327 (2013).

[36] G. I. Bykhalo, V. N. Orlin, and K. A. Stopani, arXiv:2107.08245.

[37] Z. Wang, Z. Ren, and D. Bai, Phys. Rev. C **101**, 054310 (2020).

[38] G. R. Satchler and W. G. Love, Phys. Rep. **55**, 183 (1979).

[39] D. T. Khoa, W. von Oertzen, and A. A. Ogloblin, Nucl. Phys. A **602**, 98 (1996).

[40] P. Möller, A. J. Sierk, T. Ichikawa, and H. Sagawa, At. Data Nucl. Data Tables **109-110**, 1 (2016).

[41] B. Pritychenko, M. Birch, B. Singh, and M. Horoi, At. Data Nucl. Data Tables **107**, 1 (2016); **114**, 371 (2017).

[42] A. Saxena and V. S. Ramamurthy, Pramana **27**, 679 (1986).

[43] L. C. Chamon, B. V. Carlson, L. R. Gasques, D. Pereira, C. De Conti, M. A. G. Alvarez, M. S. Hussein, M. A. Candido Ribeiro, E. S. Rossi, Jr., and C. P. Silva, Phys. Rev. C **66**, 014610 (2002).

[44] C. N. Davids and H. Esbensen, Phys. Rev. C **61**, 054302 (2000).

[45] K. Wildermuth and Y. C. Tang, *A Unified Theory of the Nucleus* (Academic Press, New York, 1977).

[46] P. Mohr, Phys. Rev. C **73**, 031301(R) (2006).

[47] M. Ismail, A. Y. Ellithi, A. Adel, and M. A. Abbas, Eur. Phys. J. A **58**, 225 (2022).

[48] Y. Ren and Z. Ren, Nucl. Sci. Tech. **24**, 50518 (2013).

[49] National Nuclear Data Center, https://www.nndc.bnl.gov.

[50] F. G. Kondev, M. Wang, W. J. Huang, S. Naimi, and G. Audi, Chin. Phys. C **45**, 030001 (2021).

[51] S. Y. Mezhevych, A. T. Rudchik, K. Rusek, A. Budzanowski, B. Czech, J. Choiński, L. Głowacka, S. Kliczewski, E. I. Koshchy, V. M. Kyryanchuk *et al.*, Nucl. Phys. A **753**, 13 (2005).

[52] Y. Gao, J. Dobaczewski, M. Kortelainen, J. Toivanen, and D. Tarpanov, Phys. Rev. C **87**, 034324 (2013).

[53] A. Soylu and C. Qi, Nucl. Phys. A **1013**, 122221 (2021).

[54] J. Dobaczewski, W. Nazarewicz, and P. G. Reinhard, J. Phys. G **41**, 074001 (2014).

[55] R. Bonetti, C. Chiesa, A. Guglielmetti, C. Migliorino, A. Cesana, and M. Terrani, Nucl. Phys. A **556**, 115 (1993).